J. Fluid Mech. (2009), *vol.* 634, *pp.* 245–268.
doi:10.1017/S0022112009007319 Printed in the United Kingdom

A family of helically symmetric vortex equilibria

DAN LUCAS† AND DAVID G. DRITSCHEL
Mathematical Institute, University of St Andrews, North Haugh, St Andrews KY16 9SS, UK

(Received 1 July 2008 and in revised form 19 March 2009)

We present a family of steadily rotating equilibrium states consisting of helically symmetric vortices in an incompressible inviscid irrotational unbounded fluid. These vortices are described by contours bounding regions of uniform axial vorticity. Helical symmetry implies material conservation of axial vorticity (in the absolute frame of reference) when the flow field parallel to vortex lines is proportional to $(1+\epsilon^2 r^2)^{-1/2}$, where ϵ is the pitch and r is the distance from the axis. This material conservation property enables equilibria to be calculated simply by a restriction on the helical stream function. The states are parameterized by their mean radius and centroid position. In the case of a single vortex, parameter space cannot be fully filled by our numerical approach. We conjecture multiply connected contours will characterize equilibria where the algorithm fails. We also consider multiple vortices, evenly azimuthally spaced about the origin. Stability properties are investigated numerically using a helical CASL algorithm.

1. Introduction

The generation of helical tip vortices in rotor wakes is of major significance in the study of many applications of propeller and wind turbine flow dynamics. Recent research has highlighted the importance of such wakes trailing wind turbines and the subsequent consequences of strong tip vortices interacting with other turbines in the wind farm (Okulov & Sørensen 2007; Walther *et al.* 2007). These studies model the wake by a system of N tip vortices, which are infinitely long slender helical vortices, equally azimuthally spaced and an additional axial hub vortex.

Widnall (1972) was the first to consider the linear stability of a helical vortex filament by calculating the self-induced velocities due to sinusoidal perturbations of the filament. Studies presented by Okulov (2004), Fukumoto & Okulov (2005) and Okulov & Sørensen (2007) have continued this procedure of evaluating the induced velocity field and have extended it to a multiplicity of vortices to address the problem of the rotor wake. Such research has remained predominately asymptotic and has been concerned almost exclusively with vortex filaments of small core radius, e.g. $R_{core} \ll d_{cen}$, where d_{cen} is the distance from the centre of the filament from the central axis.

Despite this recent interest in helical vortex stability, there has been no general theory to enable a complete description of helical vortex equilibria of arbitrary size. In a classical paper in fluid dynamics, Norbury (1973) computed, numerically, equilibria for the axisymmetric problem of a vortex ring. This class of equilibria is parameterized by a mean core radius, and each equilibrium state consists of a single closed contour

† Email address for correspondence: danl@mcs.st-and.ac.uk

bounding a distribution of azimuthal vorticity which is proportional to r, the distance from the axis of symmetry of the ring. Axisymmetric vortex rings are amongst the most widely studied fluid dynamical structures and have a multitude of applications, both in physical problems and as mathematical constructs.

This work aims to adapt Norbury's approach and apply it to that of helical vortices. We make use of helical symmetry to compute equilibria of constant pitch ($\epsilon = 1$) by considering a cross-section of constant height z and parameterizing the family of equilibria not only by a mean radius $\bar{R}$ of arbitrary size but also by a centroid position d, which can also be considered as the radius of the vortex system (in applications to wind turbine wakes, d is the rotor radius). We find that for such helically symmetric flows, and for a special choice of the velocity component parallel to vortex lines, we have material conservation of axial vorticity ω in an absolute frame of reference (such conservation was first noticed by Dritschel (1991) but ω was not identified with axial vorticity). An interesting study worthy of mention by Alekseenko *et al.* (1999) also notices this conservation. We may thus consider a contour bounding a uniform distribution of ω for which a constant helical stream function ψ upon this boundary in a rotating frame of reference implies an equilibrium state. The two main problems posed by this approach are in inverting a linear helical operator $\mathscr{L}\psi$ to compute velocities upon the contour and also in parameterizing the contour itself. The former is performed via a combination of spectral methods and finite differences and the parameterization uses a particularly effective 'time-travel' coordinate.

In the first instance we consider the case of single-vortex equilibrium states and then extend our method to N equally spaced vortices in azimuthal angle.

2. Helical symmetry

Let us consider an unbounded, inviscid, incompressible fluid which possesses helical symmetry (Landman 1990; Dritschel 1991), i.e. invariant to rotation and translation. We are able to reduce the problem to two dimensions by considering a cylindrical polar description (r, θ, z) and introducing the helical coordinate $\phi = \theta + \epsilon z$. Here ϵ is the pitch of the helix taken in our equilibria computations to be $\epsilon = 1$ without loss of generality ($\epsilon = 0$ recovers two-dimensional flow, $\epsilon \to \infty$ the axisymmetric case and $\epsilon = 1$ represents a helix which performs a single twist in an axial distance of 2π, see figure 1). We now introduce the helical vector $\boldsymbol{h}$ defined as orthogonal to ∇r and $\nabla\phi$:

$$\boldsymbol{h} = h^2(\boldsymbol{e}_z - \epsilon r \boldsymbol{e}_\theta),$$
$$h^2 = (1 + \epsilon^2 r^2)^{-1}.$$

Helical symmetry now implies that velocity, vorticity and pressure do not vary with $\boldsymbol{h}$ and $\boldsymbol{h}\cdot\nabla$ applied to any scalar function of r, ϕ and time t is zero. We may then define the unit vector for the helical coordinate ϕ by

$$\boldsymbol{e}_\phi = h^{-1}\boldsymbol{h} \times \boldsymbol{e}_r = h(\boldsymbol{e}_\theta + \epsilon r \boldsymbol{e}_z),$$

which reduces the gradient operator to $\nabla = \boldsymbol{e}_r \partial/\partial r + \boldsymbol{e}_\phi (rh)^{-1} \partial/\partial\phi$. We are now able to decompose the velocity and vorticity fields in terms of helical scalar functions

$$\boldsymbol{u} = \boldsymbol{h} \times \nabla\psi + \boldsymbol{h}\upsilon, \tag{2.1}$$
$$\boldsymbol{\omega} = \boldsymbol{h} \times \nabla\chi + \boldsymbol{h}\zeta, \tag{2.2}$$

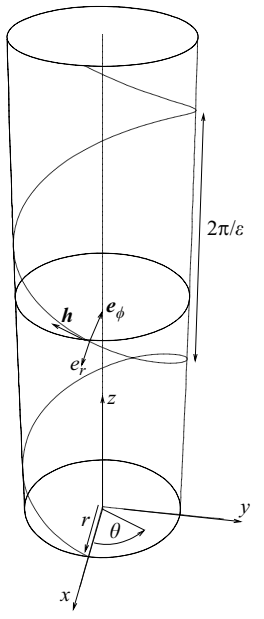

FIGURE 1. Schematic of the helical coordinate system. Note that the vectors $\boldsymbol{h}$ and $\boldsymbol{e}_\phi$ lie on the surface of the cylinder $r =$ constant. For the special class of flows considered, the vorticity $\boldsymbol{\omega}$ is everywhere tangent to $\boldsymbol{h}$.

which automatically enforces the incompressibility and divergence-free vorticity conditions. The individual velocity components can be expressed as

$$u_r = -\frac{1}{r}\frac{\partial \psi}{\partial \phi}, \tag{2.3}$$

$$u_\theta = h^2\left(\frac{\partial \psi}{\partial r} - \epsilon r \upsilon\right), \tag{2.4}$$

$$u_z = h^2\left(\upsilon + \epsilon r \frac{\partial \psi}{\partial r}\right). \tag{2.5}$$

The definition of vorticity $\boldsymbol{\omega} = \nabla \times \boldsymbol{u}$ furnishes us with the well-known helical equation coupling vorticity and velocity (Landman 1990; Dritschel 1991):

$$\mathscr{L}\psi \equiv \frac{1}{r}\frac{\partial}{\partial r}\left(rh^2\frac{\partial \psi}{\partial r}\right) + \frac{1}{r^2}\frac{\partial^2 \psi}{\partial \phi^2} = \omega + 2\epsilon h^4 \upsilon, \tag{2.6}$$

where $\omega = \boldsymbol{h}\cdot\boldsymbol{\omega} = h^2\zeta$. We must also have that $\chi = -\upsilon$.

We seek steadily rotating vortex solutions in a flow which is irrotational as $r \to \infty$ (in fact the flow will be rotational only within one or several helical vortex tubes). To this end it is convenient to express the flow in a rotating frame of reference (ω_R, υ_R, ψ_R, etc.):

$$\boldsymbol{\omega} = \boldsymbol{\omega}_R + 2\boldsymbol{\Omega},$$
$$\boldsymbol{u} = \boldsymbol{u}_R + \boldsymbol{\Omega} \times \boldsymbol{x},$$

where $\boldsymbol{\Omega} = \Omega \boldsymbol{e}_z$ is the rotation rate (to be chosen so that the flow is steady in this frame). Taking the scalar product of $\boldsymbol{h}$ with these equations gives

$$\boldsymbol{h} \cdot \boldsymbol{\omega} \equiv \omega = \omega_R + 2\Omega h^2 = \omega_R + \bar{\omega}(r),$$
$$\boldsymbol{h} \cdot \boldsymbol{u} = h^2 \upsilon = h^2 \upsilon_R + \boldsymbol{h} \cdot (\boldsymbol{\Omega} \times \boldsymbol{x}) = h^2 \upsilon_R - \epsilon r^2 h^2 \Omega,$$

i.e. $\upsilon = \upsilon_R - \epsilon r^2 \Omega = \upsilon_R + \bar{\upsilon}(r)$.

Similarly, we can express the stream function as $\psi = \psi_R + \bar{\psi}(r)$ and use (2.6) to derive $\bar{\psi}(r)$:

$$\mathscr{L}\bar{\psi}(r) = \bar{\omega}(r) + 2\epsilon h^4 \bar{\upsilon}(r) = 2\Omega h^4,$$

and solving for $\bar{\psi}(r)$ gives

$$\bar{\psi}(r) = \frac{1}{2}\Omega r^2, \tag{2.7}$$

given that we require bounded velocities.

Now turning to the full nonlinear dynamical equations in the rotating frame we have from Dritschel (1991),

$$\frac{\partial \upsilon_R}{\partial t} + J(\psi_R, \upsilon_R) = -2\epsilon\Omega \frac{\partial \psi_R}{\partial \phi}, \tag{2.8}$$

$$\frac{\partial \omega_R}{\partial t} + J(\psi_R, \omega_R) = 2\epsilon\Omega h^2 \frac{\partial \upsilon_R}{\partial \phi} + 2\epsilon h^4 \left(J(\psi_R, \upsilon_R) - \epsilon \upsilon_R \frac{\partial \upsilon_R}{\partial \phi} \right), \tag{2.9}$$

where $J(f, g)$ is the Jacobian, defined in helical coordinates as

$$J(f, g) = \frac{1}{r} \left(\frac{\partial f}{\partial r}\frac{\partial g}{\partial \phi} - \frac{\partial g}{\partial r}\frac{\partial f}{\partial \phi} \right),$$

and the terms proportional to Ω in (2.8) and (2.9) account for the effect of background rigid rotation.

Rewriting (2.8) and (2.9) in terms of the absolute frame variables υ and ω, we find

$$\frac{\partial \upsilon}{\partial t} + J(\psi_R, \upsilon) = 0, \tag{2.10}$$

$$\frac{\partial \omega}{\partial t} + J(\psi_R, \omega) = 2\epsilon h^4 \left(J(\psi, \upsilon) - \epsilon \upsilon \frac{\partial \upsilon}{\partial \phi} \right). \tag{2.11}$$

Hence, for the special case $\upsilon =$ constant, considered henceforth, it follows that the quantity ω is *materially conserved*:

$$\frac{D\omega}{Dt} \equiv \frac{\partial \omega}{\partial t} + J(\psi_R, \omega) = 0. \tag{2.12}$$

For a general helically symmetric flow with bounded momentum, it can be shown that υ must in fact be equal to the conserved circulation multiplied by $-\epsilon/2\pi$. This is a non-trivial result and will be discussed in further detail in § 3. Since $\chi = -\upsilon =$ constant in (2.2), we can express the full vorticity field in terms of ω:

$$\boldsymbol{\omega} = \omega \boldsymbol{e}_z - \epsilon r \omega \boldsymbol{e}_\theta. \tag{2.13}$$

Note that $\boldsymbol{\omega}$ is everywhere tangent to $\boldsymbol{h}$. It is the conservation of ω in (2.12) which provides us with a means to compute equilibria consisting of a contour bounding a uniform distribution of ω in a constant z cross-section and irrotational flow in the absolute frame away from the vortex. Each equilibrium state must then satisfy

$J(\psi_R, \omega) = 0$, i.e. for a single contour, the quantity $\psi_R = \psi - \frac{1}{2}\Omega r^2$ must be constant on the contour.

3. Inverting $\mathscr{L}\psi$

Having determined the prescription for an equilibrium state in terms of the helical stream function ψ we are faced with the task of accurately inverting the helical operator $\mathscr{L}\psi$. In this section we present a numerical method based on both Fourier transforms and finite differences to perform this inversion for a general distribution of axial vorticity. In addition we verify the method against an analytic solution for a particular distribution of ω.

The first step is to express ψ and ω as Fourier series in ϕ:

$$\psi = \sum_m \hat{\psi}_m(r) e^{im\phi} \qquad \text{and} \qquad \omega = \sum_m \hat{\omega}_m(r) e^{im\phi},$$

allowing us to rewrite (2.6) as

$$\tilde{\mathscr{L}}_m \hat{\psi}_m = \frac{d}{dr}\left(rh^2 \frac{d\hat{\psi}_m}{dr}\right) - \frac{m^2}{r}\hat{\psi}_m = r\hat{\omega}_m, \tag{3.1}$$

for $m > 0$. Numerically, we are able to use the fast Fourier transform algorithm (with 512 wavenumbers) to transfer between physical and spectral space in this way, and hence solve (3.1) for each azimuthal wavenumber $m > 0$ by approximating the equation by central differences (we address the $m = 0$ case later). In doing this we obtain a symmetric tridiagonal system of difference equations, easily inverted via the Thomas algorithm. To solve for large radii a novel approach is employed whereby we divide the radial grid in two parts, with a uniform grid close to the origin and a stretched grid, scaled by h, for large radius, enabling increased accuracy for smaller r. Specifically, we use the coordinates

$$\begin{aligned} r \qquad & r < r_m, \\ s = b + crh \qquad & r > r_m, \end{aligned}$$

where r_m is the grid transition radius, chosen such that the vorticity is fully contained within this radius. We integrate (3.1) up to $s = s_m = c + b$ corresponding to $rh = 1$, i.e. $r = \infty$. The constants c and b are given by continuity conditions at r_m:

$$\left.\frac{ds}{dr}\right|_{r=r_m} = 1 \quad \Rightarrow \quad c = h_m^{-3},$$

$$s_m = r_m \quad \Rightarrow \quad b = r_m(1 - ch_m) = -\epsilon r_m^3,$$

so $s = h_m^{-3} rh - \epsilon r_m^3$. In the calculations to follow a total of 400 intervals in r and s are used and a comparison with an analytic test solution is presented in Appendix A.

We now turn attention to the problem of the axisymmetric ($m = 0$) mode ψ_{axi}, and first note that we are able to decompose this mode into a υ-independent part $\hat{\psi}_0$ and a υ-dependent part ψ_υ:

$$\psi_{axi} = \hat{\psi}_0 + \psi_\upsilon,$$

where ψ_υ satisfies

$$\frac{d}{dr}\left(rh^2 \frac{d\psi_\upsilon}{dr}\right) = 2\epsilon\upsilon rh^4,$$

which we can solve directly to give

$$\psi_\upsilon = \frac{1}{2}\upsilon\epsilon r^2, \tag{3.2}$$

given that we require bounded velocities at the origin.

Now for large r we can rewrite our expression for the axial velocity (2.5) purely in terms of the axisymmetric mode (since the contribution from all other modes tends to zero in this limit):

$$\lim_{r\to\infty} u_z = \lim_{r\to\infty}\left\{\upsilon + \epsilon r h^2 \frac{\mathrm{d}\hat{\psi}_0}{\mathrm{d}r}\right\}.$$

In order for the axial momentum of the system to remain bounded we require that this limit goes to zero and we can satisfy this constraint by setting

$$\upsilon = -\lim_{r\to\infty} \epsilon r h^2 \frac{\mathrm{d}\hat{\psi}_0}{\mathrm{d}r}, \tag{3.3}$$

a constant. It is possible to relate this constant to another conserved quantity, namely circulation, defined as

$$\Gamma \equiv \int\int_A \omega \mathrm{d}A = \oint_C \boldsymbol{u}\cdot\mathrm{d}\boldsymbol{x}$$

(this is conserved due to material conservation of ω and incompressibility). Here C is a contour sufficiently large to bound all the vorticity. Substituting in the velocity components (2.3) and (2.4) and considering a contour for constant z we can express circulation as

$$\Gamma = \oint_C rh^2\left(\frac{\partial\psi}{\partial r} - \epsilon r\upsilon\right)\mathrm{d}\phi - \oint_C \frac{1}{r}\frac{\partial\psi}{\partial\phi}\,\mathrm{d}r.$$

Consider now a circular contour of radius $r\to\infty$. Noting that for large r the stream function ψ becomes independent of ϕ, since in this region $\omega = 0$, we find

$$\Gamma = 2\pi\lim_{r\to\infty}\left(rh^2\frac{\mathrm{d}\hat{\psi}_0}{\mathrm{d}r}\right) = -\frac{2\pi\upsilon}{\epsilon} \quad\Rightarrow\quad \upsilon = -\frac{\epsilon\Gamma}{2\pi}$$

using (3.3). Considering now the calculation for the complete axisymmetric stream function we first make the following observations. From (3.1) for $m=0$ we can write

$$rh^2\frac{\mathrm{d}\hat{\psi}_0}{\mathrm{d}r} = \int_0^r r'\hat{\omega}_0(r')\,\mathrm{d}r', \tag{3.4}$$

which tends to $\Gamma/2\pi$ for $r\to\infty$. We can now add the contribution from ψ_υ, having substituted for υ into (3.2), and rewrite (3.4) as the difference of two integrals (from 0 to ∞ minus from r to ∞) giving

$$\begin{aligned} rh^2\frac{\mathrm{d}\psi_{axi}}{\mathrm{d}r} &= \frac{\Gamma}{2\pi}(1-\epsilon^2r^2h^2) - \int_r^\infty r'\hat{\omega}_0(r')\,\mathrm{d}r', \\ \Rightarrow\quad \frac{\mathrm{d}\psi_{axi}}{\mathrm{d}r} &= \frac{\Gamma}{2\pi r} - \frac{1}{rh^2}\int_r^\infty r'\hat{\omega}_0(r')\,\mathrm{d}r', \end{aligned}$$

showing that $\mathrm{d}\psi_{axi}/\mathrm{d}r$ tends to 0 as $r\to\infty$ like $\Gamma/2\pi r$. Numerically, we use the equivalent expression obtained by adding (3.4) and $\mathrm{d}\psi_\upsilon/\mathrm{d}r$:

$$\frac{\mathrm{d}\psi_{axi}}{\mathrm{d}r} = S_0(r),$$

where

$$S_0(r) = \frac{1}{rh^2}\int_0^r r'\hat{\omega}_0(r')\,\mathrm{d}r' - \frac{\epsilon^2 r\Gamma}{2\pi},$$

which we have already shown tends to $\Gamma/2\pi r$ as $r \to \infty$. Integrating S_0 with respect to r produces a logarithmic singularity as $r \to \infty$. To avoid this numerically, the singularity is treated explicitly by adding and subtracting the function

$$f(r) \equiv \frac{\epsilon^2 r h^2 \Gamma}{2\pi},$$

from the right-hand side, using

$$f(r) = -\frac{\Gamma}{2\pi}\frac{\mathrm{d}\log h}{\mathrm{d}r},$$

leading to

$$\psi_{axi} = \frac{\Gamma}{2\pi}\log h + \int_r^\infty (f(r') - S_0(r'))\,\mathrm{d}r'.$$

Now both the integrand and the integral are finite for all radii. We proceed by this technique in our numerical inversion, computing the integral via the trapezoidal rule.

4. Computing equilibrium states

Having discussed the method of computing the helical stream function we are now able to address the problem of computing the equilibrium states. As mentioned in § 2 the equilibrium states are those for which $\psi - \frac{1}{2}\Omega r^2$ is constant upon a contour bounding a uniform distribution of ω. We now consider the problem in terms of a contour with $z = 0$, i.e. a vertical cross-section and consider such a contour bounding a region of uniform axial vorticity $\omega = 1$.

We expand the constraint on ψ about the previous iteration or 'basic state' and linearize, computing both the contour perturbation and angular velocity Ω at each iteration, while preserving area and centroid position. This process is repeated with the updated contour becoming the basic state until the maximum perturbation falls inside a prescribed threshold (10^{-12}) compared to the mean radius. The states are thus parameterized by the mean radius $\bar{R}$ and centroid d and the numerical algorithm spans families of states for a given $\bar{R}$ or d.

Let the new contour be $\boldsymbol{x} = \boldsymbol{x}_0 + \boldsymbol{x}'$ where $\boldsymbol{x}_0$ is the previous state and $\boldsymbol{x}'$ is a small correction. Likewise let $\Omega = \Omega_0 + \Omega'$, linearizing $\psi - \frac{1}{2}\Omega r^2 = C$ yields

$$x'v_0 - y'u_0 - \Omega_0(x_0x' + y_0y') - \frac{1}{2}\Omega'\left(x_0^2 + y_0^2\right) = C - \tilde{\psi}(x_0, y_0), \tag{4.1}$$

where

$$u_0 = -\frac{\partial}{\partial y}\psi\,(x_0, y_0)\,, \qquad v_0 = \frac{\partial}{\partial x}\psi\,(x_0, y_0)\,,$$

$$\tilde{\psi}(x_0, y_0) = \psi(x_0, y_0) - \frac{1}{2}\Omega_0\left(x_0^2 + y_0^2\right).$$

To define the contour in terms of a single variable and allow the calculation of a single perturbation quantity, we parameterize the contour following the method of Dritschel (1995) (Appendix B) whereby a normal displacement multiplied by a

'perturbation function' constitutes the disturbance, i.e.

$$\boldsymbol{x} = \boldsymbol{x}_0 + \boldsymbol{x}' = \boldsymbol{x}_0(\alpha) + \frac{\{\mathrm{d}y_0/\mathrm{d}\alpha, -\mathrm{d}x_0/\mathrm{d}\alpha\}}{(\mathrm{d}x_0/\mathrm{d}\alpha)^2 + (\mathrm{d}y_0/\mathrm{d}\alpha)^2}\eta(\alpha), \tag{4.2}$$

where η is a perturbation function. In general α can be any parameterization of the contour but here we take it to be the 'travel-time coordinate', i.e. proportional to the time taken for a fluid parcel to travel a fixed distance along the contour (for convenience $\alpha = 2\pi$ is taken as a full circuit of the contour). This parameterization simplifies the problem significantly and circumvents difficulties which arise for particularly elongated contours when using a polar type parameterization.

The basic state velocity on the contour in the rotating frame is given by

$$\tilde{\boldsymbol{u}}_0 = \frac{\partial \boldsymbol{x}_0}{\partial \alpha}\frac{\mathrm{d}\alpha}{\mathrm{d}t},$$

and $\mathrm{d}\alpha/\mathrm{d}t$ is defined by our definition for α to be

$$\frac{\mathrm{d}\alpha}{\mathrm{d}t} = \bar{\Omega},$$

where $\bar{\Omega}$ is defined as the frequency of the rotation of the fluid elements around the boundary $\boldsymbol{x}_0$. This is independent of α and implies that in a given increment of time all locations along the contour will move through the same increment of α. Thus the parameterization reduces the first three terms of (4.1), i.e.

$$\begin{aligned} x'v_0 - y'u_0 - \Omega_0(x_0x' + y_0y') &= \tilde{v}_0x' - \tilde{u}_0y' \\ &= \bar{\Omega}\eta(\alpha). \end{aligned}$$

Now (4.1) gives

$$\eta(\alpha) = \frac{1}{\bar{\Omega}}\left(C - \tilde{\psi}(x_0, y_0) + \frac{1}{2}\Omega'\left(x_0^2 + y_0^2\right)\right). \tag{4.3}$$

So we have an equation for the perturbation function in terms of the previous state $\boldsymbol{x}_0$, C and Ω'. We calculate C and Ω' from the equations for area and centroid of the contour. In terms of a contour integral we can express the area as

$$A = \frac{1}{2}\oint x\,\mathrm{d}y - y\,\mathrm{d}x.$$

Substituting our expansion $\boldsymbol{x} = \boldsymbol{x}_0 + \boldsymbol{x}'$, linearizing to first order and substituting in our time-travel coordinate parameterization (4.2) gives

$$A = A_0 + \int_0^{2\pi} \eta\,\mathrm{d}\alpha, \tag{4.4}$$

where A_0 is the area from the previous iteration. Substituting for η from (4.3) we have

$$A = A_0 + \frac{1}{\bar{\Omega}}\int_0^{2\pi}\left(C - \tilde{\psi}(x_0, y_0) + \frac{1}{2}\Omega'\left(x_0^2 + y_0^2\right)\right)\mathrm{d}\alpha. \tag{4.5}$$

The contour integral formulation for the x centroid position is given by

$$d = \frac{1}{3A}\oint x\,(x\,\mathrm{d}y - y\,\mathrm{d}x).$$

As with the area we expand in perturbation terms, linearize to first order and substitute in our parameterization (4.2) yielding

$$Ad = \frac{1}{3}\oint x_0\,(x_0\,\mathrm{d}y_0 - y_0\,\mathrm{d}x_0) + \int_0^{2\pi} x_0\eta\,\mathrm{d}\alpha,$$

and substituting for η from (4.3) gives

$$Ad = \frac{1}{3}\oint x_0\,(x_0\mathrm{d}y_0 - y_0\mathrm{d}x_0) + \frac{1}{\bar{\Omega}}\int_0^{2\pi} x_0\left(C - \tilde{\psi}(x_0, y_0) + \frac{1}{2}\Omega'\left(x_0^2 + y_0^2\right)\right)\mathrm{d}\alpha. \quad (4.6)$$

We are now able to calculate Ω' and C from (4.5) and (4.6) (effectively a 2×2 system) which in turn enables us to update the perturbation function η and thus update the contour. Numerically these integrals are evaluated using a trapezoidal rule on 400 contour points.

5. Results

Having parameterized the states in terms of a mean radius $\bar{R}$ and centroid d, we compute equilibrium states by fixing $\bar{R}$ or d and incrementing the other. Circles are provided as a first guess and convergence is generally achieved within around 20 iterations. Subsequent computations use the previous state, or an extrapolation of two previous states, as a starting point for the routine.

5.1. *The single vortex, $N = 1$*

Figure 2 shows a sample of different equilibrium states from across parameter space. These plots show the projection of the contour to form the three-dimensional helix. In particular we note that while the contour in the plane $z = 0$ can be quite elongated and curved for large d, the core of the vortex, viewed from a plane perpendicular to $\boldsymbol{h}$ (or $\boldsymbol{\omega}$), is close to circular. For smaller d we find the contours in the $z = 0$ plane are themselves closer to circular, this being nearer to the core projection. Attention is also drawn to (a) and (b) in the figure which show states of identical mean radius $\bar{R} = 2.20$ and exceptionally close centroid, $d = 0.695$ and $d = 0.696$. Despite their proximity in parameter space these states are quite distinct. Turning now to figure 3 we are able to observe where the different states lie within parameter space. Of particular importance is the region where the code fails to converge (shown as a bold line), the states mentioned above being at the lower boundary of this region. These limiting states indicate that multiply connected contours may describe the equilibria inside this region. The states on the left-hand edge of the boundary are cusp-like, for example figure 2(a), while those on the right-hand edge are more curved and elongated, e.g. figure 2(c). We conjecture that states inside the left edge will have a small hole, pinched off at this cusp, and those inside the right edge will have a larger hole, where the edges of the curved contour have 'coalesced'. These conjectures are substantiated by simulations carried out in § 5.4.

5.2. *Multiple vortices, $N > 1$*

Having examined parameter space in the case of single-vortex equilibria we extend the method to consider N evenly azimuthally spaced vortices. Clearly this implies a geometric restriction on the mean radius of the vortices dependent on the centroid radius d. We show results for the limiting states in this regime in figure 4. The contours computed show quite a degree of variation over parameter space and for small d in the cases of 2 and 3 vortices these states take on the configuration of two-dimensional

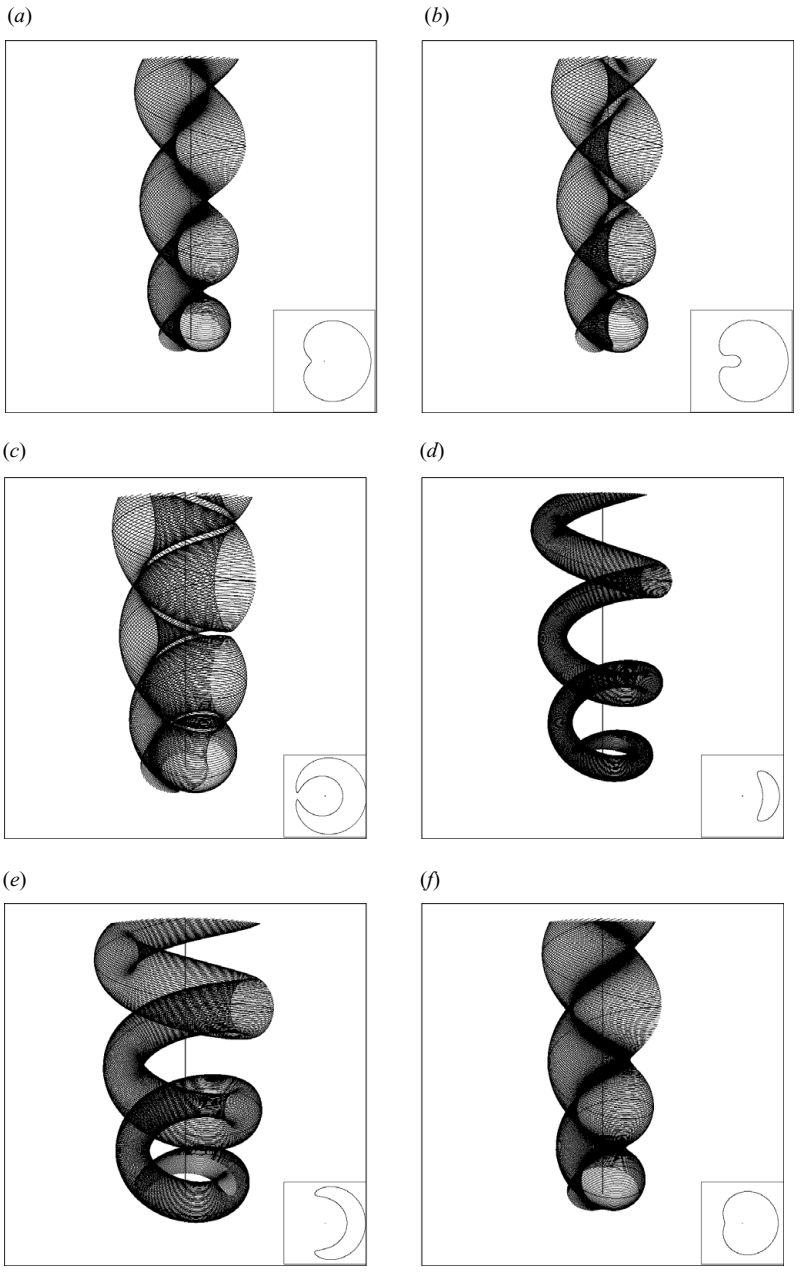

FIGURE 2. Plots of equilibrium states for a sample of parameter space: (*a*) $\bar{R} = 2.20$, $d = 0.695$; (*b*) $\bar{R} = 2.20$, $d = 0.696$; (*c*) $\bar{R} = 2.75$, $d = 0.85$; (*d*) $\bar{R} = 1.50$, $d = 2.50$; (*e*) $\bar{R} = 2.50$, $d = 2.50$; (*f*) $\bar{R} = 2.55$, $d = 0.6$. Shown are the contours along with the full three-dimensional helical vortex, viewed from a perspective of 30° elevation and 20 units from the origin. Three spirals of the helix are shown here.

corotating vortices computed by Dritschel (1985) where the limiting behaviour is for the vortices to pinch toward the origin. As d increases we see helical effects becoming more pronounced. The contours becoming increasingly curved and elongated and the

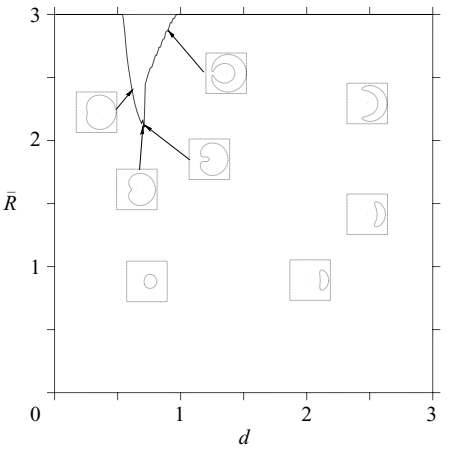

FIGURE 3. Plot of parameter space, for a single vortex, showing the boundary where convergence is not achieved with insets of equilibrium states.

vortices close up around the circle radius d. As with the single-vortex case we see contours which are closer to circular for smaller d.

Figure 5 shows parameter space for the cases of $N=2$ and $N=3$ vortices, the transition from the two-dimensional type states is notable by a distinct change in the curve showing the boundary of the limit of convergence. The states in this transition region neither close together at the origin nor around the circle, rather they flatten and form an edge facing inwards.

5.3. *Diagnostics*

In addition to axial vorticity and circulation, there are two further invariants for these flows, namely 'excess' energy E and angular impulse J per unit axial length (the axial momentum is proportional to J). The angular impulse is

$$J = \iint \omega r^2 \,\mathrm{d}x\,\mathrm{d}y = \frac{\omega}{4} \oint (x^2 + y^2)(x\,\mathrm{d}y - y\,\mathrm{d}x),$$

for a vortex patch of constant vorticity ω.

The 'excess' energy (minus an infinite constant proportional to the square of circulation) is (Dritschel 1985)

$$E \equiv -\frac{1}{2} \iint \omega \psi r \,\mathrm{d}r\,\mathrm{d}\phi,$$

conservation of which can be derived in the standard way by multiplying (2.12) by ψ and integrating. To convert this into a contour integral, we use Stokes' Theorem repeatedly to give

$$-E = \frac{1}{4}\omega \oint \left[\psi - \frac{1}{r} g h^2 \frac{\partial \psi}{\partial r} + \frac{\omega}{8}\left(r^2 + \frac{1}{3}\epsilon^2 r^4\right)\right] r^2 \,\mathrm{d}\phi + \frac{1}{4}\omega \oint \frac{g}{r}\frac{\partial \psi}{\partial \phi}\,\mathrm{d}r,$$

where

$$g(r) = \frac{1}{2}r^2 + \frac{1}{4}\epsilon^2 r^4.$$

These integrals are computed using cubic interpolation of the contours together with a two-point Gaussian quadrature method in each of the 400 intervals. This enables an accurate estimation of J and E over the entire parameter space. The calculations

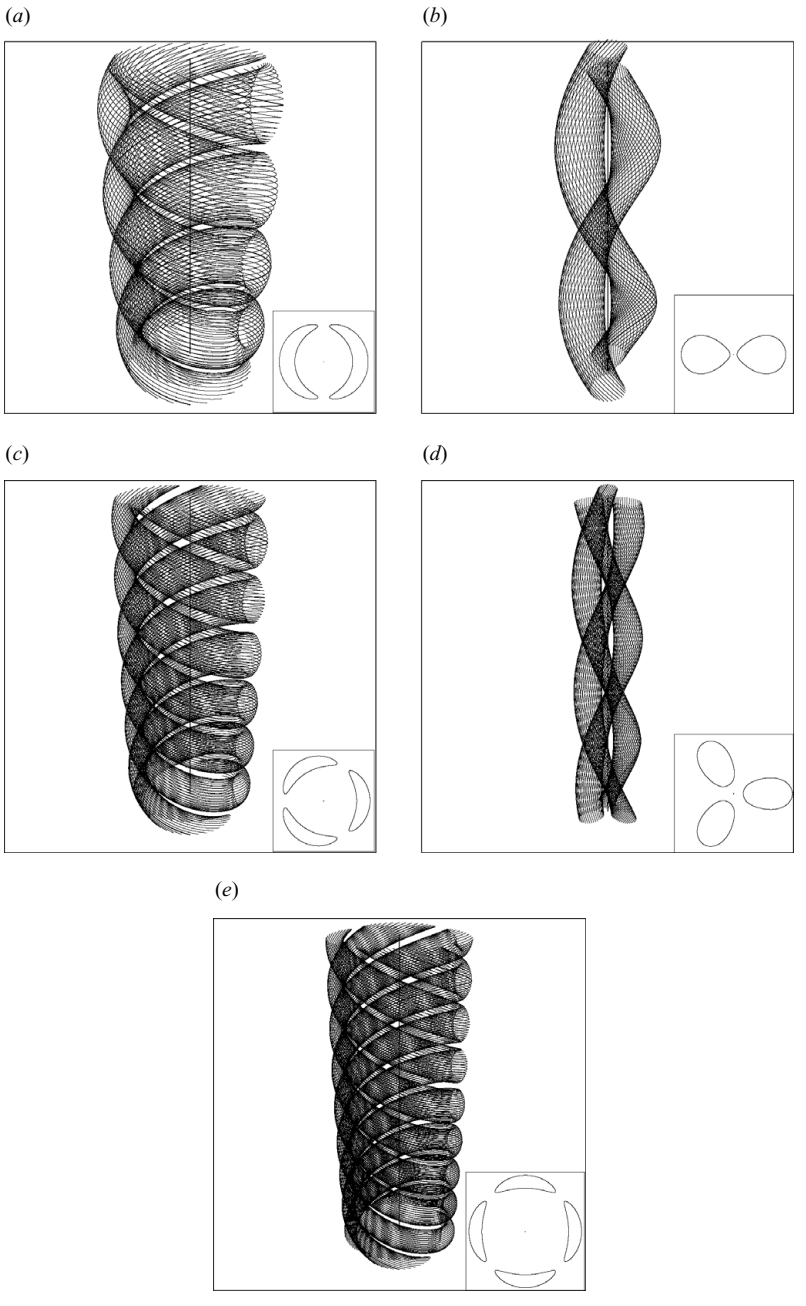

FIGURE 4. Plots of equilibrium states showing typical limiting states for $N = 2$, 3 and 4 vortices: (*a*) $N = 2$, $\bar{R} = 1.34$, $d = 2$; (*b*) $N = 2$, $\bar{R} = 0.355$, $d = 0.50$; (*c*) $N = 3$, $\bar{R} = 0.82$, $d = 2$; (*d*) $N = 3$, $\bar{R} = 0.2$, $d = 0.36$; (*e*) $N = 4$, $\bar{R} = 0.6$, $d = 2$. Contours are shown along with the full three-dimensional helical vortex viewed from the same perspective as in figure 2, with plots (*a*), (*c*) and (*e*) showing two full twists and (*b*) and (*d*) showing a single twist of the helix.

of energy and angular impulse were verified by noting that for a circular patch of constant vorticity the expressions reduce to $E = \frac{1}{4}R^4\pi(\frac{1}{4} - \log R)$ and $J = \frac{1}{2}\pi R^2$ (independent of ϵ, where R is the radius of the patch).

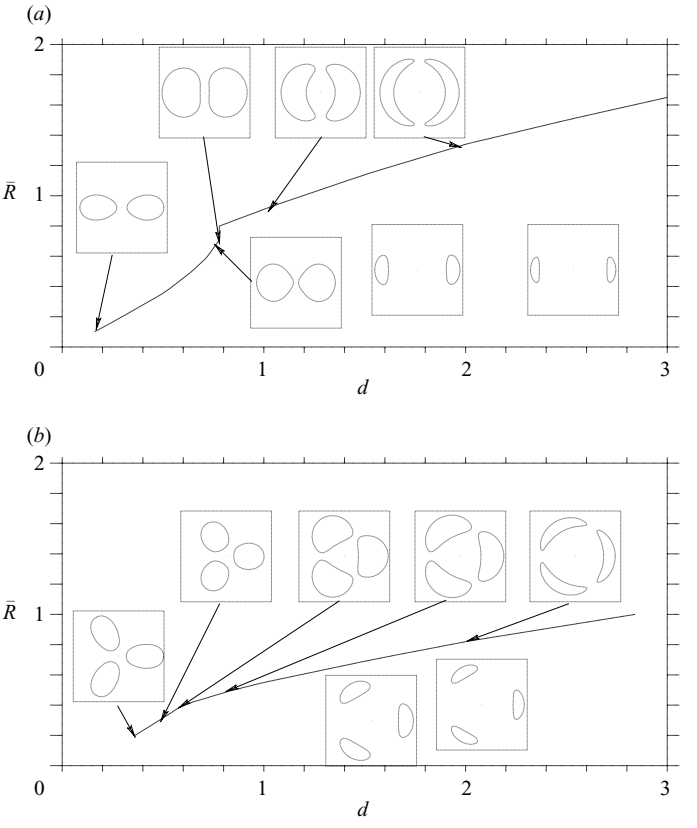

FIGURE 5. Plots of parameter space for $N = 2$ (a) and $N = 3$ (b) vortices showing the boundary where convergence is not achieved with insets of equilibrium states.

The energy, angular impulse and rotation rate of the single-vortex states are shown in figure 6. These quantities confirm that there is a jump in the nature of the states over the gap in parameter space. This is not unexpected as we have already observed a clear distinction in the shapes of the limiting states, c.f. figure 3.

Validation of the numerics has been carried out to check the computed values for rotation rate by considering small-amplitude waves on an axisymmetric helical vortex in Appendix B. It is worth mentioning that the dispersion relationship is not that of Kelvin (1880), who considered a Rankine vortex with only axial vorticity. Here helical symmetry implies we have an additional azimuthal component of vorticity (see (2.13)), and hence an associated axial flow. Further corroboration has been sought by comparing with the asymptotic approximation derived by Widnall (1972). This comparison however suffers from several limitations. First, the asymptotic approximation considers filaments of small core radius and small pitch, a regime in which our numerical computations are most sensitive to numerical error. Second, the approximation contains a correction term which requires much extra work to compute and which is simply read from the plot in Widnall (1972) in more recent work (see, e.g. Ricca 1994). The result is poor agreement. For $d = 0.5$, ignoring the correction term (a small negative contribution for $\epsilon = 1$), we have at $\bar{R} = 0.12$, $\Omega = -0.0091$ compared with Widnall's approximation $\Omega_W = -0.0085$, while

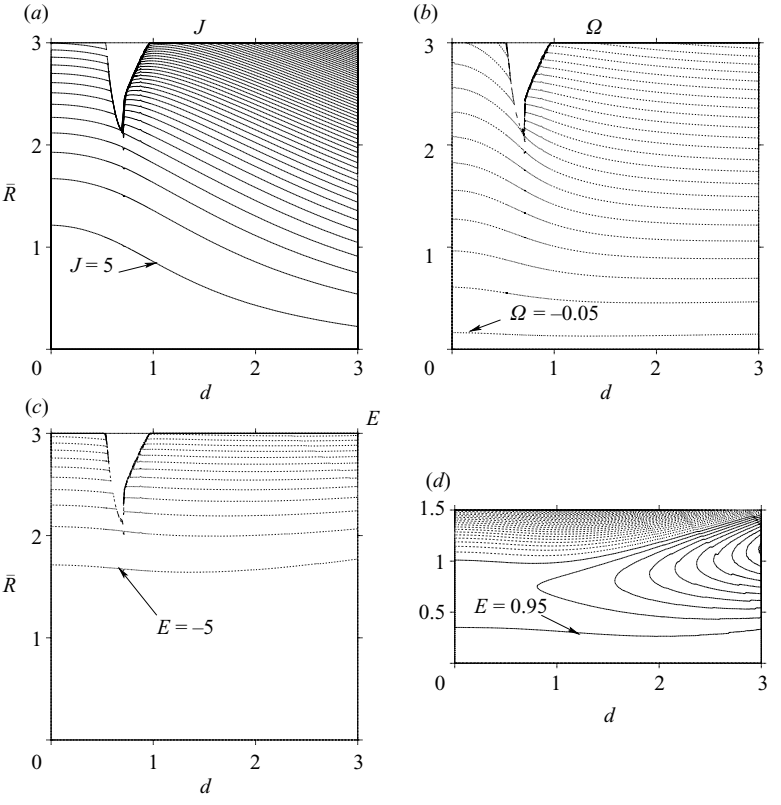

FIGURE 6. Contours of diagnostics for $N = 1$. (a) shows angular impulse J, (b) angular velocity Ω and lower plots excess energy E. Contour intervals are $\Delta J = 10$, $\Delta\Omega = 0.1$ and $\Delta E = 10$ for global energy plot (c) and $\Delta E = 0.1$ for lower half-plane plot (d).

for $\bar{R} = 0.18$, $\Omega = -0.018$ compared with $\Omega_W = -0.015$ (where Ω_W is the rotational frequency of Widnall (1972). A more convincing validation is given in Appendix B.

Figure 6(d) also shows energy contours in the lower half of parameter space. It has previously been observed in two-dimensional flows (Dritschel 1995) that an extremum of energy and angular impulse in parameter space may coincide with the margin of stability for vortex equilibria. In particular this extremum must occur over states which have equivalent circulation, in this case, for a given $\bar{R}$. Figure 6 shows a shallow minimum for increasing $\bar{R}$. These is no corresponding extremum in J, by contrast to two-dimensional flows, and direct numerical simulations of perturbed equilibria have yet to indicate any instability.

In the case of multiple vortices, we compare states with equal total circulation Γ in order to compare like states. This requires that if the mean radius of the single-vortex equilibrium is $\bar{R}_1$ then the N vortex case has the individual mean radii scaled by $1/\sqrt{N}$ so that the total area of the patches is equal (i.e. $\bar{R}_N = \bar{R}_1/\sqrt{N}$). Of particular interest in figure 7 is a reversal in the rotation rate for small d, $\bar{R}_1$ when $N > 1$. Hence there are equilibrium states for which Ω is zero. We also observe that increasing the circulation brings the trend for the single vortex closer to that of the multiple vortex case, where we have a noticeable steepening for small d.

We have attempted to compare our results for Ω with the asymptotic slender vortex results derived by Okulov (2004). Again comparisons are difficult due to the small

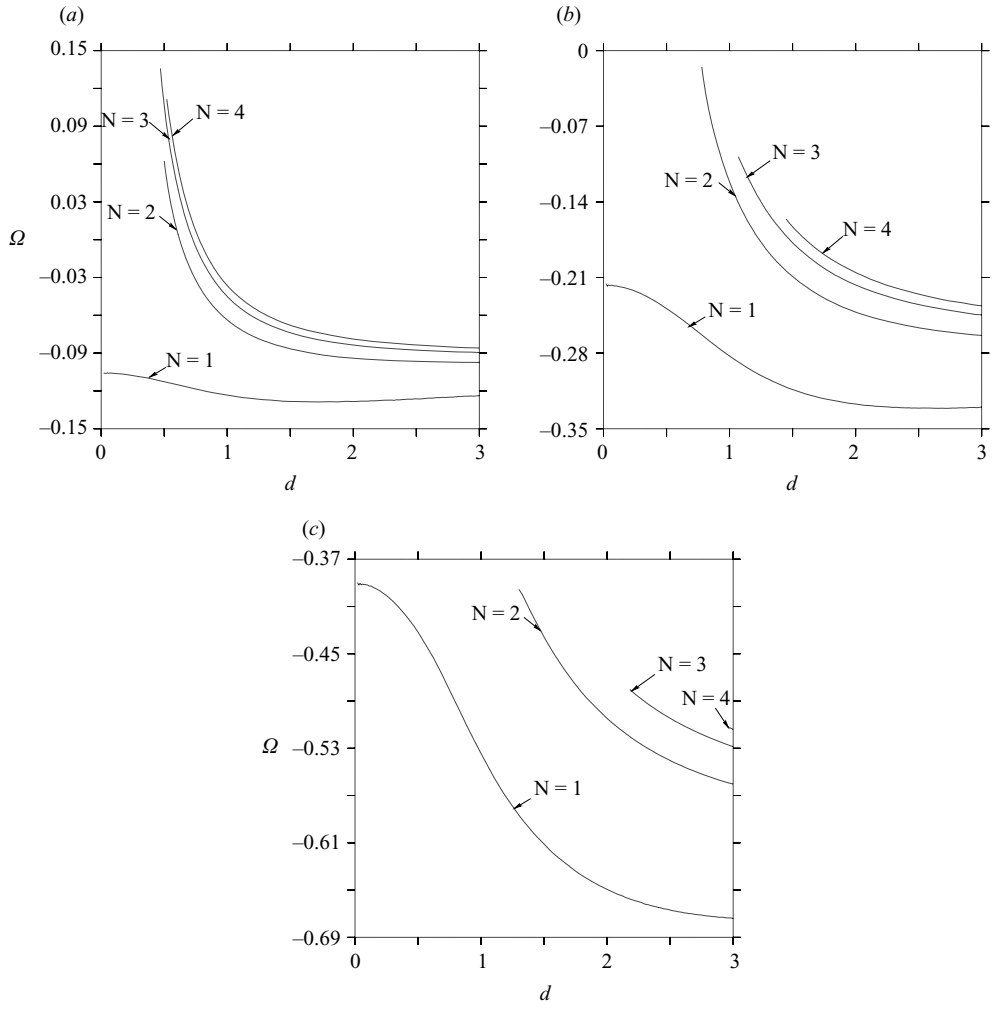

FIGURE 7. Plots of rotation rate Ω for fixed circulation or total area A_1 with curves for $N = 1$, 2, 3 and 4; (*a*) $A_1 = \pi/4$ ($\bar{R}_1 = 1/2$); (*b*) $A_1 = \pi$ ($\bar{R}_1 = 1$) and (*c*) $A_1 = 9\pi/4$ ($\bar{R}_1 = 3/2$).

core size but also due to limitations in the asymptotics. Okulov tabulates values of non-dimensional rotation rate minus a constant containing a logarithmic singularity as the core radius goes to zero. This constant term is actually of leading order and compromises the accuracy of any comparison. Nonetheless comparisons can be made; premultiplying Ω with $-4\pi d^2/\Gamma$ to be consistent with the non-dimensionalization in Okulov and considering $N = 2$, $d = 1$ and $\bar{R} = 0.15$, we find $\Omega = 0.97$ for the dimensionless rotation rate compared with $\Omega_O = 1.097$ in Okulov after reintroducing the logarithmic term. Similarly considering $\bar{R} = 0.12$ with other parameters fixed we find $\Omega = 1.04$ compared with $\Omega_O = 1.02$. In both examples the logarithmic term is $O(1)$.

5.4. *CASL simulations*

This section presents results from dynamical simulations carried out using an adapted CASL algorithm whereby contours of ω are advected by the flow field computed by inverting $\mathscr{L}\psi$ as discussed in § 3 of this paper. The reader is referred to the papers

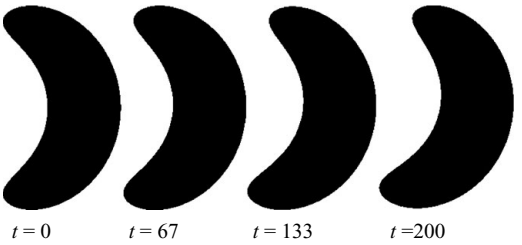

FIGURE 8. CASL simulation for the $N = 1$, $\bar{R} = 2$, $d = 2$ state with perturbation $\Delta d = 0.01$.

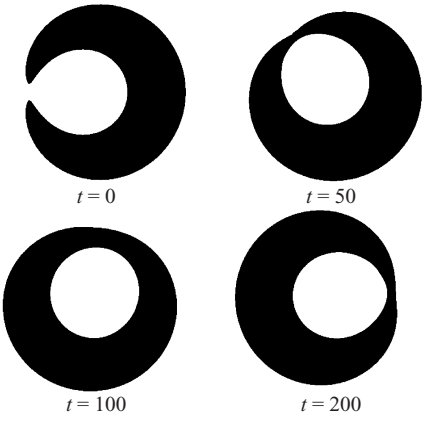

FIGURE 9. CASL simulation for the $N = 1$, $\bar{R} = 2.64$, $d = 0.8$ state with perturbation $\Delta d = -0.03$.

of Dritschel & Ambaum (1997) and Macaskill, Padden & Dritschel (2003) for a more detailed description of the model. Although this model limits one to the purely helical evolution of vorticity, we are able to deduce the validity of our equilibrium states and their stability (to spatial perturbations) under helical symmetry (and for $v = \text{constant}$). In addition we are able to validate the conjectures made regarding the gap in parameter space when $N = 1$.

Simulations are carried out with a time step $\Delta t = 0.025$ (the CASL algorithm uses a standard fourth-order Runge–Kutta time integration) together with 400 radial intervals and 512 azimuthal intervals. The equilibria are perturbed by displacing all the x coordinates of the contour nodes by some increment Δd. All figures shown in this section are in the rotating frame of the equilibrium state.

Figure 8 shows a generic single-vortex equilibrium state, $\bar{R} = 2$, $d = 2$ perturbed by a small amount $\Delta d = 0.01$. Virtually no effect is felt by the vortex, even at late times. The only dynamical response is a slight change in the rotation rate.

Figures 9 and 10 show simulations for $N = 1$ where limiting states at the boundary in parameter space are perturbed in the direction of the gap. Figure 9 shows an elongated contour from the right edge of the gap, closing over and cutting off a region of zero vorticity within the vortex edge. Hence the equilibrium evolves into a multiply connected state. Figure 10 shows the entrainment of filamentary structures of irrotational fluid into the vortex. For large time, the filaments congregate into a small region of zero vorticity inside the vortex. These simulations provide compelling evidence that multiply-connected equilibrium states exist in the gap. Notably, despite

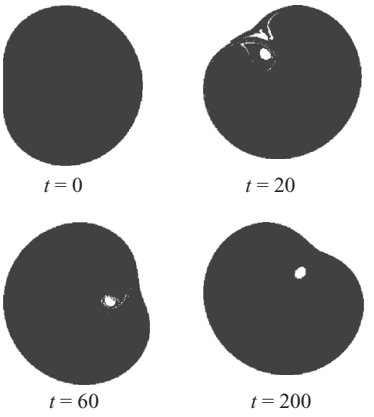

FIGURE 10. CASL simulation for the $N = 1$, $\bar{R} = 2.2$, $d = 0.6$ state with perturbation $\Delta d = 0.1$.

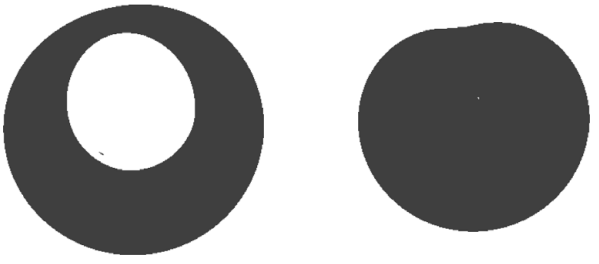

FIGURE 11. Final frame for CASL simulation, $t = 200$, left-hand plot shows the $\bar{R} = 2.64$, $d = 0.8$ state with perturbation $\Delta d = -0.105$ and the right the $\bar{R} = 2.64$, $d = 0.59$ state with perturbation $\Delta d = 0.105$.

the distinct change in the shape of the contour, the vortices remain coherent and robust. In the case shown in figure 10 filaments entrained inside the vortex coalesce into a single patch of zero vorticity inside the vortex. The changes in topology occur through the removal of extremely thin filaments by 'surgery' (Dritschel 1988) at a tenth of the inner radial spacing of the grid. This allows the vortex to relax to a quasi-steady state while only very weakly dissipating angular impulse and energy.

To gain a more comprehensive picture of the interior states, simulations were carried out perturbing the edge states from either side of the gap by an equal and opposite amount. This gives the evolution of two different states of the same mean radius at the same centroid location d. Figure 11 shows the final frame for large time of these simulations for the limiting states at $\bar{R} = 2.64$ and suggests that there is the possibility that more than one equilibria state exists for a particular point of parameter space inside the gap. It is conceivable that multiply-connected equilibria exist anywhere in parameter space, not solely in this region where we were unable to find singly connected states.

As previously suggested, these single-vortex states are remarkably stable to finite-amplitude perturbations. To demonstrate this, we performed a simulation where the equilibrium for $\bar{R} = 1$ and $d = 1$ was perturbed by $\Delta d = 1$, i.e. a full doubling of the centroid. Figure 12 shows the flow evolution. Although the contour deforms strongly and has a substantial anomaly in its angular velocity, it remains coherent after only tiny filaments have been expelled.

FIGURE 12. CASL simulation for the $N = 1$, $\bar{R} = 1$, $d = 1$ state with perturbation $\Delta d = 1$.

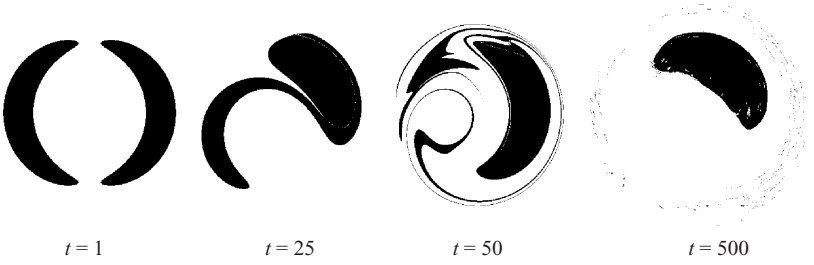

FIGURE 13. CASL simulation for the $N = 2$, $d = 2$, $\bar{R} = 1.34$ state with perturbation $\Delta d = 0.01$.

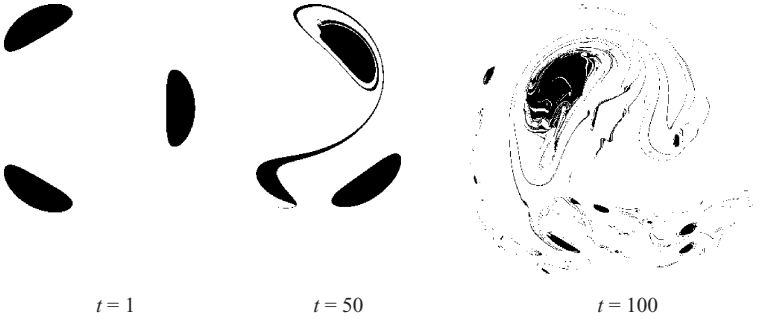

FIGURE 14. CASL simulation for $N = 3$, $d = 2$, $\bar{R} = 0.5$ state with perturbation $\Delta d = 0.01$.

In contrast to the strong stability of the single-vortex states, the multiple-vortex states present more varied results. Generally it is found that the vortex states for $\bar{R} \ll d$ are more robust than those for which $\bar{R} \approx d$. Perturbing states in which the vortices are larger and more closely spaced, we observe that the rotation rates of the individual patches diverge from the rotation rate of the system, causing the patches to move together and interact. Figures 13, 14 and 15 show this for $N = 2$, 3 and 4 vortices, respectively. The long-time behaviour, in particular for the two vortex case, shows the vorticity tending towards a single patch type configuration, as we have observed to be stable in helical dynamics.

6. Conclusions

This paper has presented a numerical method for computing equilibrium states for helically symmetric vortices. A novel approach using Fourier transforms and finite differences on a two-part grid was employed to invert the linear operator $\mathscr{L}\psi$ for a general distribution of axial vorticity. A property which has proved crucial in allowing the computation of these equilibrium states is that helically symmetric flows

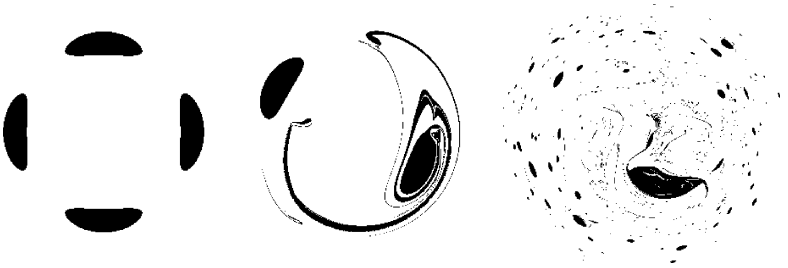

FIGURE 15. CASL simulation for $N = 4$, $d = 2$, $\bar{R} = 0.5$ state with perturbation $\Delta d = 0.01$.

materially conserve axial vorticity when the flow parallel to vortex lines is proportional to $(1+\epsilon^2 r^2)^{-1/2}$. Moreover, the constant of proportionality is uniquely determined by the integral of axial vorticity over a cross-section $z = \text{constant}$ (the circulation), by the requirement of bounded momentum per unit length. Equivalently, this conservation property follows from restricting the vorticity to be everywhere tangent to the helical vector $\boldsymbol{h}$.

Here we have computed equilibria described by contours bounding regions of uniform axial vorticity $\omega = 1$. The equilibria depend only on their radius and centroid position. The contours are parameterized by a time-travel coordinate to allow arbitrary distortions. In the single-vortex case we have been able to compute equilibrium states over all of parameter space apart from a specific region where we conjecture only multiply-connected states exist. CASL simulations support this conjecture and also demonstrate the remarkable stability of the states. It should be noted, however, that this stability is for purely helical dynamics and previous asymptotic results (Widnall 1972) suggest that instability would likely occur in the full three-dimensional dynamics.

In the case of multiple vortices we have computed equilibrium states over parameter space and determine where geometric constraints prevent equilibria. We see a distinction between the states for small radial spacing d, where we have a configuration analogous to the two-dimensional vortex equilibria of Dritschel (1985), and the states for moderate or large radial spacing, where helical effects become important. Simulations show helical instability for larger, more closely spaced configurations, with the long time evolution tending towards a single patch configuration.

When considering equilibrium vortex configurations, one must entertain the possibility that there exists a multiplicity of states for a fixed location in parameter space. In the case of a single two-dimensional Rankine vortex patch we now know that there is an infinite multiplicity of states arising from the linear displacement modes proportional to $e^{im\theta}$ (see Saffman 1992). When $m = 2$, these states are elliptical (Kirchhoff 1876). These elliptical states have a self-induced rotation, $\Omega = \omega\lambda/(1+\lambda)^2$, associated with them which is dependent upon the aspect ratio λ of the patch. Analogous states almost certainly exist also in helical flows, for vortices centred on the z-axis (see Appendix B). In helical flows an additional rotation is induced by the curved shape of the vortex as it twists around the z-axis. If we now consider, as in this work a single vortex *not* centred on the z-axis but displaced from it by a small distance d, an equilibrium in some rotating frame of reference requires that the self-induced rotation (for $d = 0$) nearly matches the rotation of the curved vortex about the z-axis. This additional requirement for helical flows suggests that the vortex shape is unique for a given dimensionless mean radius $\epsilon\bar{R}$ and displacement ϵd. We

hence conjecture that there are no other single-vortex equilibria for $\epsilon d > 0$ than the ones we have found here.

We motivated this work by the recent studies on rotor wake flows (Okulov & Sørensen 2007; Walther *et al.* 2007) and many parameters commonly associated with such applications can easily be represented by the parameters used here (noting first that setting $\epsilon = 1$ sets the length scale of the system). Parameters such as rotor radius d and pitch ϵ are readily available and the circulation of each vortex has been discussed in § 3 and is proportional to $\bar{R}^2$. The advance ratio, commonly utilized in aerodynamics, defined as the ratio of the velocity of the flow over the rotor to the angular velocity of the rotor, can be expressed here as simply $1/d\epsilon$ (velocity of flow over the rotor can be expressed as $2\pi/\epsilon T$ and angular velocity $2\pi d/T$ where T is the period of rotation). Although the problem of the rotor wake is not directly addressed in this work, care has been taken to ensure that the size, strength and configurations of vortices considered are of such a general nature as to be applicable to a variety of applications.

The problem of the rotor wake can be more fully addressed in future work by adapting this method to include a central hub vortex consistent with the rotor wake configuration. This introduces two additional parameters to the problem, namely the strength and size of the inner vortex. Also of interest is to extend the method to consider multiply connected patches of vorticity.

The equilibrium states found in this paper can be adapted for use as non-trivial test cases in the simulation of the three-dimensional Euler equations and are a step more complex than Norbury's vortex rings. We plan to use these states to test a new hybrid Lagrangian–Eulerian algorithm for the three-dimensional Euler equations.

Dan Lucas would like to acknowledge the support of the School of Mathematics and Statistics at the University of St Andrews and also the C. K. Marr Educational Trust for jointly funding this research.

Appendix A. Analytic solution

It is possible to construct analytic solutions to (3.1) via the use of Green's functions for the case of circular, compact distributions of $\hat{\omega}$, corresponding to $\omega = \hat{\omega}(r)\mathrm{e}^{\mathrm{i}m\phi}$. Following the general theory of Green's functions we seek a solution of the form

$$\hat{\psi}(r) = \int_0^\infty G(r\,;r_0) r_0 \hat{\omega}(r_0)\,\mathrm{d}r_0,$$

where G is Green's function and satisfies the homogeneous equation $\tilde{\mathscr{L}}G = 0$ (see (3.1), here we take $\epsilon = 1$ consistent with the results presented). It can be shown that Green's function has the form

$$G(r\,;r_0) = \begin{cases} r r_0 I_m'(mr) K_m'(mr_0) & r < r_0 \\ r r_0 K_m'(mr) I_m'(mr_0) & r > r_0 \end{cases},$$

where I_m and K_m are the modified Bessel functions of the first and second kind, of order m, and a prime denotes a derivative with respect to the argument.

Consider an idealized axial vorticity defined by

$$\hat{\omega}(r) = \begin{cases} 1 & r < R \\ 0 & r > R \end{cases},$$

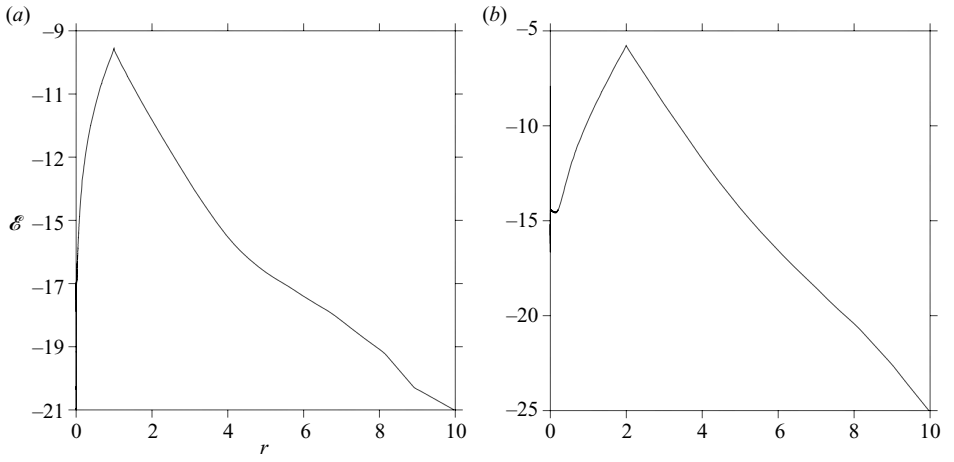

FIGURE 16. Plots showing difference in the numerical calculation of $\hat{\psi}$ and the analytic solution (A 1) ($\mathscr{E} = \log_{10}|\hat{\psi}_{ana} - \hat{\psi}_{num}|$) for a circular distribution with radius $R = 1$, wavenumber $m = 2$ (a) and radius $R = 2$, wavenumber $m = 3$ (b).

for a circular cross-section, radius R. Then the stream function becomes

$$\hat{\psi} = \begin{cases} -rK'_m(mr)\int_0^r r_0^2 I'_m(mr_0)\mathrm{d}r_0 - rI'_m(mr)\int_r^R r_0^2 K'_m(mr_0)\mathrm{d}r_0 & r < R \\ -rK'_m(mr)\int_0^R r_0^2 I'_m(mr_0)\mathrm{d}r_0 & r > R \end{cases}. \tag{A 1}$$

This analytic solution for $\hat{\psi}$ allows the numerical inversion to be accurately verified for this particular distribution of axial vorticity.

Figure 16 displays plots showing the difference between the analytically computed solution (e.g. (A 1) with integrals computed via a midpoint rule), and the numerically computed solution computed on the two part grid as described in § 3. We have very good agreement and suffer partial loss in accuracy across the boundary of the circular vortex patch.

Appendix B. Dispersion relation for a columnar vortex with helical symmetry

Over a century ago Lord Kelvin calculated the dispersion relationship for infinitesimal linear perturbations of a uniform vortex column (Kelvin 1880). The non-axisymmetric azimuthal disturbances with azimuthal wavenumber $m = 1$ are known as bending modes and correspond to helical disturbances of the vortex. This work was generalized by Moore & Saffman (1972) to include an axial flow which subsequently became the starting point for many asymptotic studies of a helical vortex filament, e.g. Ricca (1994), Kuibin & Okulov (1998). Linear stability of a Rankine vortex with a discontinuous axial flow and the addition of swirl has been considered by Loiseleux, Chomaz & Huerre (1998) who computed frequencies for the helical bending modes. It is, however, possible to generalize this linear theory yet further by considering an axisymmetric columnar vortex with helical symmetry.

Starting from linear theory we expand about the basic state. We note that, due to the presence of azimuthal vorticity ($\boldsymbol{\omega} = \omega \boldsymbol{e}_z - \epsilon r\omega \boldsymbol{e}_\theta$), there is a parabolic axial flow within the undisturbed vortex given by $\bar{u}_z = \frac{1}{2}\omega\epsilon(r^2 - R^2)$. Note also that $\bar{u}_z = 0$ outside the vortex. Due to material conservation of ω, (2.12), we can restrict attention

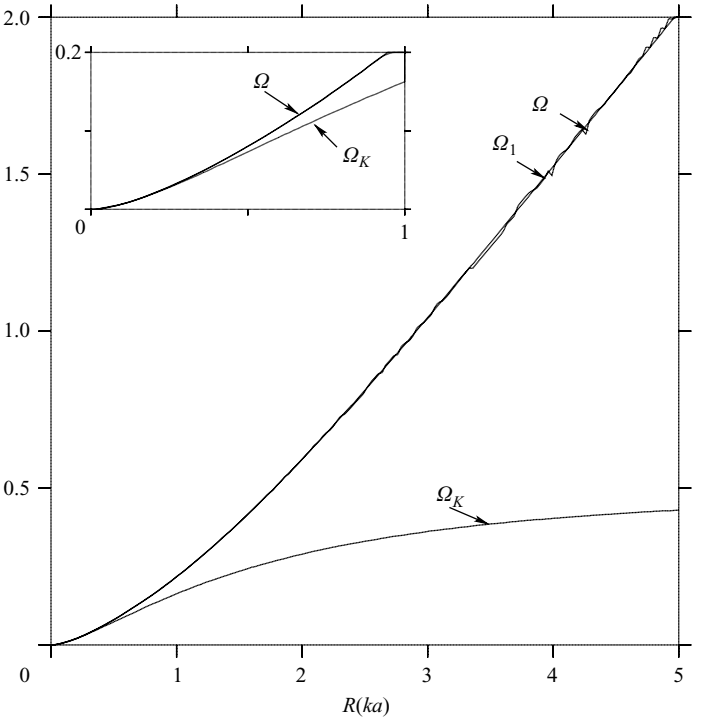

FIGURE 17. Curves showing the numerically computed rotation rate Ω (for $d = 0.02$) and the analytical bending mode frequencies, Ω_1 and Ω_K, of a perturbed axisymmetric helical and rectilinear vortex, respectively, against non-dimensional wavenumber $\epsilon R = R$ or ka.

to deformations of the vortex edge in the plane $z = 0$. This implies that the perturbation vorticity $\omega' = 0$ both inside and outside the vortex boundary. The linearized version of (2.6) then gives simply $\mathscr{L}\psi' = 0$, and expressing $\psi' = \Re(\sum_m \hat{\psi}_m(r)\mathrm{e}^{\mathrm{i}m\theta - \mathrm{i}\sigma t})$ we have solutions to the homogeneous problem as given in Appendix A, namely

$$\hat{\psi}_m = AG(r; R), \tag{B 1}$$

where G is Green's function and A is a constant to be determined by matching the velocity components at the boundary.

Defining the perturbed vortex edge as $r = R + \eta(\theta, t)$, where R is the radius of the undisturbed vortex, we use the fact that η evolves materially according to

$$\frac{Dr}{Dt} = u_r \quad \Rightarrow \quad \frac{D\eta}{Dt} = u_r \quad \Rightarrow \quad \frac{\partial \eta}{\partial t} + \frac{u_\theta}{r}\frac{\partial \eta}{\partial \theta} = u_r.$$

Rewriting η as $\eta = \Re(\sum_m \hat{\eta}_m \mathrm{e}^{\mathrm{i}m\theta - \mathrm{i}\sigma t})$ we obtain after linearization

$$\left(\frac{1}{2}\omega m - \sigma\right)\hat{\eta}_m = -\frac{m}{R}\hat{\psi}_m(R) = -mA\frac{G(R; R)}{R}, \tag{B 2}$$

given the simple form of the velocity field for an axisymmetric uniform helical vortex.

We now require the velocity field to be continuous on the perturbed boundary $r = R + \eta$. The radial component consists only of a perturbed part and is continuous over r by the continuity of $\hat{\psi}_m$. The azimuthal component has a mean part whose shear jumps across the boundary. Continuity of the full azimuthal component then

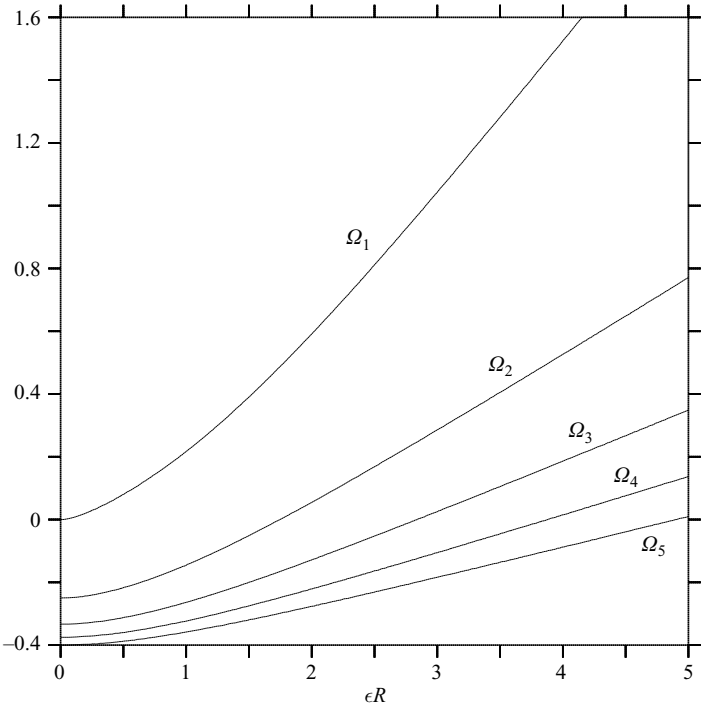

FIGURE 18. Curves showing the analytical linear mode frequencies, Ω_1 to Ω_5, of a perturbed axisymmetric helical vortex against non-dimensional wavenumber ϵR.

implies a jump in the perturbed part, i.e. $[u'_\theta] = \omega\eta$, at $r = R$, upon linearization. This implies

$$\omega\hat{\eta}_m = h^2(R)\left[\frac{\mathrm{d}\hat{\psi}_m}{\mathrm{d}r}\right] \qquad \Rightarrow \qquad \omega\hat{\eta} = \frac{A}{R}, \tag{B 3}$$

from (B 1) and Appendix A. Continuity of axial velocity yields the same relationship.

Substituting (B 3) into (B 2) leads to the dispersion relation

$$\Omega_m = -\frac{\sigma}{m\omega} = -\frac{1}{2} + (\epsilon R)^2 I'_m(m\epsilon R)K'_m(m\epsilon R), \tag{B 4}$$

where we have now restored the dependence on pitch. In our analysis ϵ is the direct analogue of the axial wavenumber k and ϵR is a dimensionless axial wavenumber (denoted ka in Saffman 1992) The dispersion relation (B 4) is not the same as the one derived by Kelvin (1880) who assumed a two-dimensional (non-helical) basic state with $\boldsymbol{\omega} = \omega\boldsymbol{e}_z$ in contrast to $\boldsymbol{\omega} = \omega\boldsymbol{e}_z - \epsilon r\omega\boldsymbol{e}_\theta$ in helical flows.

This expression for Ω_m furnishes us with a further validation of our numerics. For $m = 1$, (B 4) gives an approximation for the rotation rate Ω (for $\omega = 1$), in the regime $d \ll 1$. Figure 17 shows Ω_1 from (B 4) versus the numerically computed Ω (for $d = 0.02$), together with the rotational frequency obtained by Kelvin (1880) against dimensionless axial wavenumber. Notice that despite considering a more complex flow, the dispersion relation derived here is much simpler than Kelvin's, allowing the precessional frequency of the vortex to be directly calculated without having to solve a transcendental equation. The curves for Ω_1 and Ω indicate very close agreement of

the numerical computations and the linear theory. These curves diverge from Kelvin's as axial wavenumber increases and the vortex lines become less rectilinear.

The angular frequencies of the linear helical modes, $\Omega_m(\epsilon R)$ for $m = 1$ to 5 are plotted in figure 18 (for $\omega = 1$). For $\epsilon R \ll 1$, these tend to the two-dimensional values $\frac{1}{2}(m-1)/m$, while for $\epsilon R \gg 1$, these tend to $\frac{1}{2}\epsilon R/m$. The existence of these modes implies that there are finite-amplitude non-axisymmetric helical vortex equilibria also for $m > 1$ centred on the z-axis.

REFERENCES

Alekseenko, S. V., Kuibin, P. A., Okulov, V. L. & Shtork, S. I. 1999 Helical vortices in swirl flow. *J. Fluid Mech.* **382**, 195–243.

Dritschel, D. G. 1985 The stability and energetics of corotating uniform vortices. *J. Fluid Mech.* **157**, 95–134.

Dritschel, D. G. 1988 Contour surgery: a topological reconnection scheme for extended integrations using contour dynamics. *J. Comput. Phys.* **77** (1), 240–266.

Dritschel, D. G. 1991 Generalized helical Beltrami flows. *J. Fluid Mech.* **222**, 525–541.

Dritschel, D. G. 1995 A general theory for two-dimensional vortex interactions. *J. Fluid Mech.* **293**, 269–303.

Dritschel, D. G. & Ambaum, M. H. P. 1997 A contour-advective semi-Lagrangian algorithm for the simulation of fine-scale conservative fields. *Q. J. R. Meteorol. Soc.* **123**, 1097–1130.

Fukumoto, Y. & Okulov, V. L. 2005 The velocity field induced by a helical vortex tube. *Phys. Fluids* **17** (107101).

Kelvin, Lord 1880 Vibrations of a columnar vortex. *Phil. Mag.* **10**, 155–168.

Kirchhoff, G. 1876 *Vorlesungen über mathematische Physik*. Mechanik.

Kuibin, P. A. & Okulov, V. L. 1998 Self-induced motion of helical vortices. In *IUTAM Symposium on Dynamics of Slender Vortices*, pp. 55–62.

Landman, M. J. 1990 On the generation of helical waves in circular pipe flow. *Phys. Fluids* A **2**, 738–747.

Loiseleux, T., Chomaz, J. M. & Huerre, P. 1998 The effect of swirl on jets and wakes: linear instability of the rankine vortex with axial flow. *Phys. Fluids* **10**, 1120–1134.

Macaskill, C., Padden, W. E. P. & Dritschel, D. G. 2003 The CASL algorithm for quasi-geostrophic flow in a cylinder. *J. Comput. Phys.* **488**, 232–251.

Moore, D. W. & Saffman, P. G. 1972 The motion of a vortex filament with axial flow. *Phil. Trans. R. Soc. Lond.* A **272**, 403–429.

Norbury, J. 1973 A family of steady vortex rings. *J. Fluid Mech.* **57** (3), 417–431.

Okulov, V. L. 2004 On the stability of multiple helical vortices. *J. Fluid Mech.* **521**, 319–342.

Okulov, V. L. & Sørensen, J. N. 2007 Stability of helical tip vortices in a rotor far wake. *J. Fluid Mech.* **576**, 1–25.

Ricca, R. L. 1994 Effect of torsion on vortex filament motion. *J. Fluid Mech.* **273**, 241–259.

Saffman, P. G. 1992 *Vortex Dynamics*. Cambridge University Press.

Walther, J. H., Guènot, M., Machefaux, E., Rasmussen, J. T., Chatelain, P., Okulov, V. L., Sørensen, J. N., Bergdorf, M. & Koumoutsakos, P. 2007 A numerical study of the stability of helical vortices using vortex methods. In *The Science of Making Torque from Wind*, *Journal of Physics: Conference Series*, vol. 75.

Widnall, S. E. 1972 The stability of a helical vortex filament. *J. Fluid Mech.* **54** (4), 641–663.